A time-continuous approach to analyzing anode aging in solid-oxide fuel cells via stochastic 3D microstructure modeling and physics-based simulations

Sabrina Weber[1], Benedikt Prifling[1], Ravi Kumar Jeela[2], Andreas Prahs[3], Daniel Schneider[2,3],

Britta Nestler[2,3], Volker Schmidt[1]

[1]*Institute of Stochastics, Ulm University, 89069 Ulm, Germany*
[2] *Institute of Digital Materials Science, University of Applied Science Karlsruhe, 76012 Karlsruhe, Germany*
[3] *IAM - Microstructure Modelling and Simulation, Karlsruhe Institute of Technology, 76131 Karlsruhe, Germany*

Abstract

Solid-oxide fuel cells (SOFCs) are a promising energy conversion technology, offering a low environmental impact, low costs and high flexibility regarding the choice of the fuel. However, electrochemical performance of SOFCs decreases with time as a result of complex structural aging mechanisms of their anodes that are not yet fully understood. An option to quantitatively investigate this aging behavior could be tomographic imaging of the 3D microstructure of SOFC anodes for different aging durations, which is expensive and time-consuming. To overcome this issue, physics-based aging simulations resolving the 3D microstructural evolution can be exploited, which use tomographic image data of pristine SOFC anodes consisting of nickel, gadolinium-doped ceria (GDC) and pore space, as initial state. This microstructure simulation method is based on a grand-chemical potential multi-phase-field approach including surface diffusion. Computations conducted with the simulation framework are capable to predict the coarsening of the multiphase polycrystalline electrode. A promising approach to further accelerate the quantitative investigation of SOFC degradation is to combine physics-based aging simulation with data-driven stochastic 3D microstructure modeling, which is typically less computationally intensive compared to phase-field simulations. More precisely, an excursion set model based on Gaussian random fields is used to characterize the 3D microstructure of SOFC anodes by means of a small number of interpretable model parameters. Moreover, the evolution of the parameter vector of the calibrated stochastic 3D model over time is modeled by analytical functions that make fast predictive simulations possible. The prediction robustness is investigated by first assuming that the evolution of the 3D microstructure is known up to a certain point in time. Then, in a second step, the 3D microstructure of SOFC anodes is predicted for further future points in time and, through geometrical descriptors, compared with the results of physics-based aging simulation.

Keywords— solid-oxide fuel cell, stochastic microstructure model, Gaussian random field, χ^2-field, excursion set, phase-field simulation, aging behavior

1 Introduction

Solid oxide fuel cells (SOFCs) offer a promising solution for clean and efficient energy generation, combining high performance with fuel flexibility and reduced environmental impact [1, 2]. However, several studies reported some open problems such as pronounced degradation effects such as coarsening of the nickel phase [3–5]. Since the 3D microstructure of SOFC electrodes is known to significantly affect chemical performance [6, 7], a deeper understanding of its evolution over time is crucial to improving the performance and particularly the long-term behavior of SOFC electrodes. For SOFC anodes based on yttrium-stabilized zirconia (YSZ), these degradation effects have already been investigated in relation to the microstructure [8, 9]. However, in recent years, YSZ has been increasingly replaced

---

[*] Corresponding author

Email addresses: sabrina.weber@uni-ulm.de

by gadolinium-doped cerium (GDC) due to its higher ionic conductivity at lower temperatures [10–12]. Studies on GDC have also reported pronounced degradation effects, including decreasing performance and coarsening of the nickel (Ni) and GDC phases [13–16].

To characterize the temporal evolution of the 3D microstructure of SOFC anodes, experimental aging studies combined with 3D focused ion beam scanning electron microscopy (FIB-SEM) have been performed [16–18]. However, the acquisition of such high-resolution 3D images is time-consuming and expensive. In order to address this issue, physics-based aging simulations using a multiphase-field model can be exploited. In particular, multiphase-field simulations provide valuable insights into the microstructural changes and their impact on the performance of SOFCs, where the selection of a suitable model and its parameters are the most crucial steps.

In computational materials science, the phase-field method [19–22] is a well-established approach for efficiently simulating microstructure evolution [23]. Consequently, it has been widely employed on SOFC anodes [24–29], where the model considered in [30, 31] offers several advantages. It allows for the independent control of interfacial energies for each binary interface while maintaining equal, finite interfacial thicknesses and quantitatively capturing interfacial diffusion. Consequently, experimentally measured surface diffusion coefficients and wetting angles can be directly incorporated. Using this framework, the coarsening behavior in Ni-YSZ anodes has been investigated in [32] based on FIB-SEM data.

The multiphase-field studies mentioned above have primarily focused on Ni-YSZ systems, where the Ni phase evolves while the YSZ phase remains stable. In contrast, only a few studies have focused on Ni-GDC systems where both phases evolve, leading to a more complex microstructural evolution. In [33], a mesoscale model has been developed to predict the morphological and performance degradation of Ni-GDC during long-term operation. Although informative, this work relied on synthetic microstructures and performed validation against data from the literature with limited consideration of microstructural properties such as mean particle sizes and triple phase boundary density. Recently, in [34], quantitative 3D multiphase-field simulations of Ni-GDC coarsening have been performed by employing experimentally reconstructed 3D FIB-SEM microstructures, and validated them against aged samples (for aging durations of 240 h and 1100 h). Their model predictions of particle sizes, triple phase boundary density, tortuosities, and specific surface area evolutions corresponded closely to experimental results. Reliable interfacial energies and diffusion parameters, crucial for accurate degradation prediction, were derived based on a Bayesian active learning framework [35] to address the scarcity of Ni–GDC data in the literature. Furthermore, the results obtained in [34] also revealed the sensitivity of surface and interfacial energies and their impact on microstructural evolution and anode performance.

Although these physics-based aging simulations provide valuable insight, they are computationally intensive and limited in their ability to generate multiple realizations of the 3D microstructure for one and the same aging time. To overcome these challenges, we propose a hybrid approach that combines physics-based aging simulations with a stochastic modeling framework that allows one to quickly generate virtual but realistic 3D microstructures, where a promising tool from stochastic geometry to model three-phase materials are excursion sets of Gaussian random fields [36–39]. More precisely, two excursion sets based on two different Gaussian random fields model the three phases. However, Gaussian random fields are not always suitable, and more general random χ^2-fields can be used instead [40, 41]. Such stochastic 3D models can be characterized by a few interpretable parameters, which allows for so-called virtual material testing by systematically varying the model parameters and thus generating a large number of virtual but realistic 3D microstructures [42–45]. In the present paper, an excursion set model based on a χ^2-field and a Gaussian random field with six parameters is used to model the 3D microstructure of SOFC anodes, which consists of GDC, nickel and pore space, for various aging durations. The model is calibrated using analytical formulas that describe the relationships between the model parameters and two geometrical descriptors, namely the volume fraction and the two-point coverage probability function.

This low-parametric representation enables efficient investigation of the microstructure's evolution over time by calibrating the model to the 3D microstructure of SOFC anodes obtained by physics-based aging simulations. Then, non-linear regression allows us to quantitatively describe the temporal evolution of model parameters. This enables predictive simulations, i.e., to predict the 3D microstructure of an SOFC anode for an arbitrary aging duration. The accuracy of the model is evaluated by comparing geometrical descriptors computed for realizations of the stochastic model with those obtained from physics-based aging simulations. In addition, the prediction quality of the model is investigated. Furthermore, the relationship between the six model parameters and various geometrical descriptors is quantitatively analyzed for a better understanding of the model.

The remainder of this paper is organized as follows. In Section 2, the phase-field method of physics-based aging simulations is briefly explained. The stochastic 3D model together with the procedure to fit the model parameters is described in Section 3. Then, in Section 4, the results obtained with respect to model fitting, regression of model parameters, and prediction quality are presented. Moreover, the relationship between model parameters and geometrical descriptors is investigated. Section 5 concludes and provides an outlook for possible further research.

2 Numerical simulation of aging process

Conventional approaches to investigating the aging behavior of SOFC anodes are usually based on time-consuming and expensive 3D imaging for various time points to accurately capture the evolution of the 3D microstructure. To overcome this issue, numerical simulations of the aging process are used which are based on segmented tomographic image data of sample A from [15]. This data has been acquired via 3D FIB-SEM, as pristine state manufactured by the powder technology, where the resulting 3D image data of the pristine SOFC anode has a voxel size of 50 nm and a field of view of 6.4 µm × 37.0 µm × 28.2 µm.

More precisely, a multiphase-field model based on the grand-potential functional of [30], extended to include surface self-diffusion [31], is employed to simulate the coarsening of both the Ni and GDC phases under thermal operating conditions. The porous Ni–GDC anode system is represented using three distinct order parameters corresponding to the nickel phase, the GDC phase, and the pore space, respectively. Each order parameter is a continuous variable defined over the simulation domain to distinguish between different phases of the material. The distinct values of 0 and 1 represent non-existence and existence of individual bulk phases, while intermediate values denote the interface regions between the phases. Unlike Ni–YSZ anodes, where only the Ni phase evolves, Ni–GDC systems exhibit concurrent Ni and GDC coarsening [13]. Surface diffusion is considered the dominant mass transport mechanism within the typical range of SOFC operating temperatures. The model incorporates diffusion along the Ni-GDC interface, offering a more comprehensive description of mass transport pathways.

More details on model formulation, validation against experimental Ni–GDC anode data, and model parameters representing operating conditions of Ni-GDC at a temperature of 900 °C with a gas composition of H_2-50% / H_2O-50% can be found in [34, 35]. In continuation of our previous work, in which we validated the multiphase-field simulation results against experimentally aged microstructures (imaged by 3D FIB-SEM) after 240 hours and 1100 hours under thermal operating conditions [34], we now perform large-scale phase-field simulations of microstructural altering over 38 000 h in the present paper. The simulations employ an pristine Ni-GDC anode microstructure reconstructed from 3D FIB-SEM as initial input and model parameters derived from a Bayesian active learning framework [35]. The model parameters represent operating conditions of Ni-GDC at a temperature of 900 °C with a gas composition of H_2-50% / H_2O-50%. The evolution and degradation of the microstructure are predicted over time, with simulation data recorded at intervals of 500 h up to 38 000 h. For this work, a single-instruction multiple-data (SIMD) vectorized solver available in the simulation framework Pace3D [46] is used, the implementation of which is described in detail in Section 4.2 of [47].

3 Stochastic 3D microstructure modeling

In this section, the stochastic 3D model is introduced, which is used to generate virtual but realistic 3D microstructures of SOFC anodes for different aging durations. This model exhibits a small number of interpretable parameters and allows for fast predictive simulations. For calibrating and validating this model, various geometrical descriptors are used, which are briefly introduced first.

3.1 Geometrical descriptors

The geometrical descriptors considered in the present paper are summarized in Table 1. More information on these descriptors, including additional references and a description of their computation from voxelized 3D image data, can be found in [15]. Note that the double phase boundary (DPB) denotes the interface area of the GDC phase and the pore space. The DPB and the triple phase boundary (TPB) are required for the chemical reaction in the SOFC anode and are therefore particularly important descriptors of the microstructure. Moreover, due to the poor connectivity of the nickel phase, see [15], we decided to consider the mean geodesic tortuosity of the paths starting from the TPB.

Geometrical descriptor	Symbol	Range	Unit
Volume fraction	ε_i	$[0,1]$	-
Two-point coverage probability	$C_{i,j}$	$[0,1]$	-
Specific surface area (SSA)	S_i	$[0,\infty)$	μm^{-1}
Specific length of triple phase boundary (TPB)	T	$[0,\infty)$	μm^{-2}
Specific area of double phase boundary (DPB)	D	$[0,\infty)$	μm^{-1}
Mean geodesic tortuosity of paths starting from TPB	$\mu(\tau_i)$	$[0,\infty)$	-
Mean chord length	$\mu(L_i)$	$[0,\infty)$	µm

Table 1: Overview of the geometrical descriptors used for model validation. Here, $i,j \in \{\text{Ni,P, GDC}\}$ indicate the given phase, namely the Ni phase, the pore space (P), and the GDC phase.

3.2 Model description

The stochastic 3D microstructure model is based on excursion sets of random fields. In particular, we first consider two independent standardized Gaussian random fields $X = \{X(t), t \in \mathbb{R}^3\}$ and $Y = \{Y(t), t \in \mathbb{R}^3\}$. More precisely, we assume that the random variables $X(t)$ and $Y(t)$ follow the law of a univariate standard normal distribution, i.e., $\mathbb{E}X(t) = \mathbb{E}Y(t) = 0$ and $\text{Var}X(t) = \text{Var}Y(t) = 1$ for each $t \in \mathbb{R}^3$. Besides this, we assume that the Gaussian random fields X and Y are stationary and isotropic (also called motion-invariant). Under these assumptions, the distributions of X and Y are uniquely determined by the underlying covariance functions $\rho_X, \rho_Y : [0,\infty) \to [-1,1]$, which are given by $\rho_X(h) = \text{Cov}(X(s), X(t))$ and $\rho_Y(h) = \text{Cov}(Y(s), Y(t))$ for each $h > 0$, where $s, t, \in \mathbb{R}^3$ with $|s - t| = h$ and $|\cdot|$ denotes the Euclidean norm. Notice that the values of $\rho_X(h)$ and $\rho_Y(h)$ do not depend on the specific choice of s and t, due to the motion invariance of the Gaussian random fields X and Y. More details on Gaussian random fields can be found in [48–50]. In the present paper, we assume that ρ_X and ρ_Y belong to the exponential family, i.e., we assume that

$$\rho_X(h) = \exp(-(\alpha_X h)^{\beta_X}) \qquad \text{and} \qquad \rho_Y(h) = \exp(-(\alpha_Y h)^{\beta_Y}) \tag{1}$$

for each $h > 0$ and some parameters $\alpha_X, \alpha_Y \in (0,\infty)$ and $\beta_X, \beta_Y \in (0,2)$; see, e.g., [48].

However, it turns out that excursion sets of Gaussian random fields are not suitable for adequately modeling the nickel phase. As a possible way out, we consider a motion-invariant χ^2-field Z with two degrees of freedom based on the Gaussian random field X. This means that the random field $Z = \{Z(t), t \in \mathbb{R}^3\}$ is defined by $Z(t) = X_1^2(t) + X_2^2(t)$ for each $t \in \mathbb{R}^3$, where $X_1 = \{X_1(t), t \in \mathbb{R}^3\}$ and $X_2 = \{X_2(t), t \in \mathbb{R}^3\}$ are independent copies of X. Note that the covariance function $\rho_Z : [0,\infty) \to [0,4]$ of Z can easily be derived from the covariance function ρ_X by

$$\rho_Z(h) = 4\rho_X(h)^2 \tag{2}$$

for each $h > 0$, see Eq. (6.155) in [48]. Now, the three phases of the SOFC anodes can be modeled by excursion sets of the random fields Y and Z. More precisely, the nickel phase is modeled by the excursion set $\Xi_{\text{Ni}} = \{t \in \mathbb{R}^3 : Z(t) \geq \lambda_Z\}$ for some threshold parameter $\lambda_Z \in \mathbb{R}$, whereas the pore space is modeled by $\Xi_{\text{P}} = cl(\{t \in \mathbb{R}^3 : Y(t) \geq \lambda_Y\} \cap \Xi_{\text{Ni}}^{\complement})$ for some threshold parameter $\lambda_Y \in \mathbb{R}$, where cl denotes the topological closure and $A^{\complement}$ is the complement of the set $A \subset \mathbb{R}^3$. The GDC phase is given by $\Xi_{\text{GDC}} = cl((\Xi_{\text{Ni}} \cup \Xi_{\text{P}})^{\complement})$. Note that the random closed sets $\Xi_{\text{Ni}}, \Xi_{\text{P}}$ and Ξ_{GDC} are motion invariant, due to the motion invariance of the Gaussian random fields X and Y. More details on random closed sets can be found, e.g., in [48, 51].

The stochastic 3D model described above exhibits the parameter vector $\theta = (\lambda_Z, \lambda_Y, \alpha_X, \alpha_Y, \beta_X, \beta_Y)$, which can be calibrated to tomographic image data by means of analytical relationships between the parameters and geometrical descriptors of the model. In particular, we use the fact that the volume fraction ε_{Ni} of the Ni phase is given by

$$\varepsilon_{\text{Ni}} = \mathbb{P}(o \in \Xi_{\text{Ni}}) = \mathbb{P}(Z(o) \geq \lambda_Z) = 1 - F_{Z(o)}(\lambda_Z), \tag{3}$$

where $F_{Z(o)} : \mathbb{R} \to [0,1]$ is the distribution function of the χ^2-distribution with two degrees of freedom and $o = (0,0,0) \in \mathbb{R}^3$ denotes the origin [48]. Moreover, due to the independence of the random fields Y and Z, the volume fraction ε_{P} of the pore space is given by

$$\varepsilon_{\text{P}} = \mathbb{P}(Y(o) \geq \lambda_Y, Z(o) < \lambda_Z) = F_{Z(o)}(\lambda_Z) - F_{Z(0)}(\lambda_Z)F_{Y(o)}(\lambda_Y), \tag{4}$$

where $F_{Y(o)} : \mathbb{R} \to [0,1]$ denotes the distribution function of the standard normal distribution. Thus, to determine the threshold parameters λ_Y and λ_Z, the volume fractions $\varepsilon_{\mathrm{Ni}}$ and ε_{P} of the Ni phase and the pore space will be computed from the image data and inserted into Eqs. (3) and (4), see Section 3.3 below.

To determine the remaining four model parameters, two-point coverage probabilities are considered. where the two-point coverage probability function $C_{ij} : [0,\infty) \to [0,1]$ is given by $C_{ij}(h) = \mathbb{P}(o \in \Xi_i, u \in \Xi_j)$ for any pair $i,j \in \{\mathrm{Ni, P, GDC}\}$ and each $u \in \mathbb{R}^3$ such that $|u| = h \geq 0$, see [48]. In particular, we use the following relationships that, as the volume fractions $\varepsilon_{\mathrm{Ni}}$ and ε_{P} in Eqs. (3) and (4), express the two-point coverage probability functions $C_{\mathrm{Ni,Ni}}$ and $C_{\mathrm{P,P}}$ by the model parameters. Namely, as shown in [40], we have

$$C_{\mathrm{Ni,Ni}}(h) = \mathbb{P}(Z(o) > \lambda_Z, Z(u) > \lambda_Z) = 2\varepsilon_{\mathrm{Ni}} - 1 + (1 - \rho_X^2(h)) \sum_{j=0}^{\infty} \frac{\rho_X^{2j}(h)}{(j!)^2} \left(\int_0^{\frac{j}{2(1-\rho_X^2(h))}} t^j \exp(-t) dt \right)^2, \tag{5}$$

for each $u \in \mathbb{R}^3$ such that $|u| = h \geq 0$. Furthermore, from the independence of the random fields Y and Z we get

$$\begin{aligned} C_{\mathrm{P,P}}(h) &= \mathbb{P}(Y(o) > \lambda_Y, Z(o) < \lambda_Z, Y(u) > \lambda_Y, Z(u) < \lambda_Z) \\ &= (C_{\mathrm{Ni,Ni}}(h) + 2F_{Z(0)}(\lambda_Z) - 1)(1 + \mathbb{P}(Y(o) < \lambda_Y, Y(u) < \lambda_Y) - 2F_{Y(0)}(\lambda_Y)), \end{aligned} \tag{6}$$

for each $u \in \mathbb{R}^3$ such that $|u| = h \geq 0$, where the random vector $(Y(o), Y(u))$ has a bivariate standard normal distribution with covariance $\mathrm{Cov}(Y(o), Y(u)) = \rho_Y(h)$ given by Eq. (1). Thus, it applies

$$\mathbb{P}(Y(o) < \lambda_Y, Y(u) < \lambda_Y) = \int_{-\infty}^{\lambda_Y} \int_{-\infty}^{\lambda_Y} \varphi_{\rho_Y(h)}(s,t) \, \mathrm{d}s \, \mathrm{d}t, \tag{7}$$

where $\varphi_\gamma : \mathbb{R}^2 \to [0,\infty)$ is the probability density of a two-dimensional Gaussian random vector with standard normal marginal distributions and covariance $\gamma \in [-1,1]$.

3.3 Model fitting

We now show how Eqs. (3) - (7) can be used to determine the model parameters $\lambda_Z, \lambda_Y, \alpha_X, \alpha_Y, \beta_X, \beta_Y$ from voxelized and segmented image data of SOFC anodes.

Fitting procedure for each aging duration. We first describe a method to fit the model parameters λ_Z and λ_X as well as the covariance functions ρ_X and ρ_Y for each aging duration. In particular, the following steps are applied separately to each 3D image obtained by the numerical aging simulations explained in Section 2. Therefore, we first compute appropriately chosen estimators $\hat{\varepsilon}_{\mathrm{Ni}}, \hat{\varepsilon}_{\mathrm{P}}, \hat{C}_{\mathrm{Ni,Ni}}$ and $\hat{C}_{\mathrm{P,P}}$ for $\varepsilon_{\mathrm{Ni}}, \varepsilon_{\mathrm{P}}, C_{\mathrm{Ni,Ni}}$ and $C_{\mathrm{P,P}}$ from 3D image data. For estimating the volume fractions $\varepsilon_{\mathrm{Ni}}$ and ε_{P}, the so-called point-count method is used [48], whereas the two-point coverage probability functions $C_{\mathrm{Ni,Ni}}$ and $C_{\mathrm{P,P}}$ are estimated from voxelized image data with a Fourier-based method described in [52]. Then, an estimator $\hat{\lambda}_Z$ for the threshold λ_Z is obtained by solving Eq. (3) for λ_Z, i.e., $\hat{\lambda}_Z = F_{Z(o)}^{-1}(1 - \hat{\varepsilon}_{\mathrm{Ni}})$. Similarly, plugging $\hat{\lambda}_Z$ and $\hat{\varepsilon}_{\mathrm{P}}$ into Eq. (4) allows us to get an estimator $\hat{\lambda}_Y$ by solving Eq. (4) for λ_Y. Note that the distribution functions $F_{Z(o)}$ and $F_{Y(o)}$ are monotonously increasing, which allows us to numerically solve Eqs. (3) and (4) for λ_Z and λ_Y, respectively, using the bisection method [53]. Moreover, plugging $\hat{\varepsilon}_{\mathrm{Ni}}$ and $\hat{C}_{\mathrm{Ni,Ni}}(h)$ into Eq. (5) provides an estimator $\hat{\rho}_X(h)$ for $\rho_X(h)$. As noted in [40], the values of $C_{\mathrm{Ni,Ni}}(h)$ decrease monotonously with increasing $h > 0$, i.e., with decreasing values of $\rho_X(h) \in [0,1]$. Thus, we can again use the bisection method to compute $\hat{\rho}_X(h)$ for $h > 0$. In the next step, the estimators $\hat{C}_{\mathrm{P,P}}(h), \hat{C}_{\mathrm{Ni,Ni}}(h), \hat{\lambda}_Z, \hat{\lambda}_Y$ are plugged into Eq. (6). As in the case before, the right-hand side of Eq. (6) is decreasing monotonously with decreasing values of $\rho_Y(h) \in [0,1]$. Thus, taking into account Eq. (7), the bisection method can be used to get an estimate $\hat{\rho}_Y(h)$ for $\rho_Y(h)$.

However, the procedure stated above leads to non-parametric estimates $\hat{\rho}_X(h), \hat{\rho}_Y(h)$ for the covariance functions ρ_X and ρ_Y. To represent the estimated covariance functions by the exponential functions given in Eq. (1), the parameters $\alpha_X, \beta_X, \alpha_Y$ and β_Y are estimated by minimizing the mean squared error (MSE) of the non-parametric estimates $\hat{\rho}_X(h), \hat{\rho}_Y(h)$ obtained from image data and their parametric representations given in Eq. (1). More precisely, the trust region reflective algorithm [54] is used to minimize MSE.

Time-dependent regression of model parameters. Using the previously described fitting procedure for the aging durations of 0 h, 500 h, ..., 38 000 h, we obtain a parameter vector $\theta_t = (\theta_{t,1}, \ldots, \theta_{t,6}) \in \mathbb{R}^6$ for each $t \in \mathcal{T} =$

$\{0\,\mathrm{h}, 500\,\mathrm{h}, \ldots, 38\,000\,\mathrm{h}\}$. Thus, by means of non-linear regression, we are able to predict the entries of θ_t for an arbitrary specification $t \geq 0$ of the aging duration. The regression functions $f_a : [0, \infty) \to (0, \infty)$ used for this purpose depend on a four-dimensional parameter vector $a = (a_1, a_2, a_3, a_4) \in \mathbb{R}^4$ and are given by

$$f_a(t) = a_1 \exp(-a_2 t^{a_3}) + a_4, \tag{8}$$

for each $t \geq 0$. Then, for each $j \in \{1, \ldots, 6\}$, the optimal parameter vector $a_j^* \in \mathbb{R}^4$ is determined by minimizing the MSE between the values of $f_a(t)$ and the j-th model parameter $\theta_{t,j}$ for each $t \in \mathcal{T}$. More precisely, we solve the optimization problem given by

$$a_j^* = \underset{a \in \mathbb{R}^4}{\operatorname{argmin}} \sum_{t \in \mathcal{T}} (f_a(t) - \theta_{t,j})^2. \tag{9}$$

This optimization problem is numerically solved with the command *scipy.optimize.curve_fit* in Python using the trust region reflective algorithm [54] for all six model parameters.

To investigate the robustness of predictive simulations of SOFC anodes using the stochastic 3D model, we fit the regression functions $f_{a_1^*}, \ldots, f_{a_6^*}$ of the six model parameters $\theta_{t,1}, \ldots, \theta_{t,6}$ for different time intervals of aging duration. More precisely, we used the results of the physics-based aging simulation obtained for the following time intervals: $[0\,\mathrm{h}, 4000\,\mathrm{h}]$, $[0\,\mathrm{h}, 9500\,\mathrm{h}]$, $[0\,\mathrm{h}, 19\,000\,\mathrm{h}]$, $[0\,\mathrm{h}, 28\,500\,\mathrm{h}]$, and $[0\,\mathrm{h}, 38\,000\,\mathrm{h}]$. To evaluate the prediction quality of the resulting models, we use the geometrical descriptors, which have been introduced in Section 3.1.

4 Results

In this section, the results are discussed that have been obtained for fitting the stochastic 3D model introduced in Section 3.2 to image data generated by the numerical aging simulations of Section 2. In particular, in Section 4.2, the predictive potential of the regression functions is evaluated which have been introduced in Section 3.3. Finally, in Section 4.3, relationships are derived by means of which geometrical descriptors of the simulated 3D morphologies of SOFC anodes can be expressed by the parameters of the stochastic 3D model.

4.1 Evaluation of the stochastic 3D model

We first evaluate the stochastic 3D model introduced in Section 3 which has been fitted separately to each of the 77 images of SOFC anodes obtained for the aging durations of 0 h, 500 h, ..., 38 000 h by the numerical aging simulations explained in Section 2. In Figure 1, the 3D morphology of an SOFC anode is shown, which has been obtained after 500 h of physics-based aging simulations (left), together with a realization of the stochastic 3D model fitted to the aforementioned image data (right).

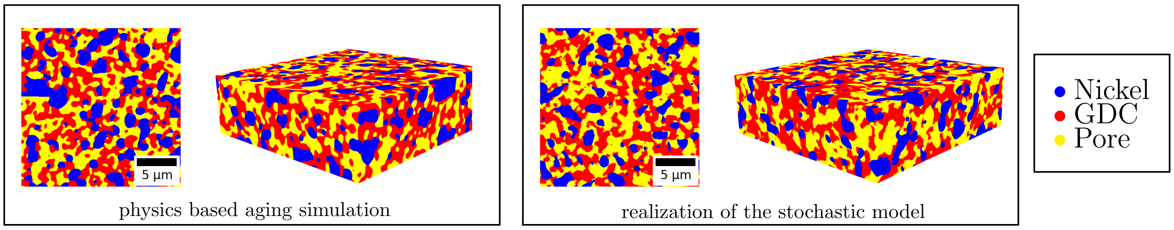
physics based aging simulation

realization of the stochastic model

Figure 1: 2D slices (20 µm × 20 µm) and 3D renderings (20 µm × 6.35 µm × 20 µm) of the 3D morphology of SOFC anodes after 500 h, consisting of nickel (blue), GDC (red) and pore space (yellow), obtained by physics-based aging simulations (left) and stochastic 3D modeling (right).

To quantitatively evaluate the stochastic 3D model for each duration of aging, 10 realizations of the model with a size of 20 µm in each direction are generated for each of the 77 aging durations considered in this paper. Then, in the next step, the volume fraction, the specific surface area (SSA), the mean geodesic tortuosity from TPB, and the mean chord length are computed for the three phases of each of these realizations. Based on these values, the mean absolute percentage error (MAPE) is determined with respect to the corresponding values computed from the 77 images of SOFC anodes generated by the physics-based aging simulations.

More precisely, for each of the four geometrical descriptors stated above, let d_t^{phy} denote the descriptor value obtained from the physics-based aging simulation at aging duration $t \in \mathcal{T}$, and let $d_{t,k}^{\text{sto}}$ be the corresponding descriptor value obtained from the k-th realization of the stochastic 3D model at $t \in T$, for each $k \in \{1, \dots, 10\}$. The results obtained for the MAPE given by

$$MAPE = \frac{1}{77} \sum_{t \in \mathcal{T}} \frac{1}{10} \sum_{k=1}^{10} \left| \frac{d_t^{\text{phy}} - d_{t,k}^{\text{sto}}}{d_t^{\text{phy}}} \right| \tag{10}$$

are shown in Table 2, where it can be seen that we get small MAPE-values in most cases. For the volume fraction, the SSA, and the mean geodesic tortuosity, the MAPE-values are below 10 % for each of the three phases. The highest MAPE-values over all 77 aging durations are obtained for the mean chord length of the nickel and GDC phases with 22.63% and 19.21%, respectively. However, for the mean chord length of the pore space, we obtain a very small MAPE-value of 2 %.

MAPE	ε_i	S_i	$\mu(\tau_i)$	$\mu(L_i)$
Nickel	0.59 %	7.23 %	4.97 %	22.63 %
Pores	0.34 %	8.21 %	5.79 %	2.05 %
GDC	0.34 %	8.98 %	3.04 %	19.21 %

Table 2: MAPE-values over all 77 aging durations for the volume fraction ε_i, the specific surface area S_i, the mean geodesic tortuosity $\mu(\tau_i)$, and the mean chord length $\mu(L_i)$ of the i-th pase, where $i \in \{\text{Ni,P,GDC}\}$.

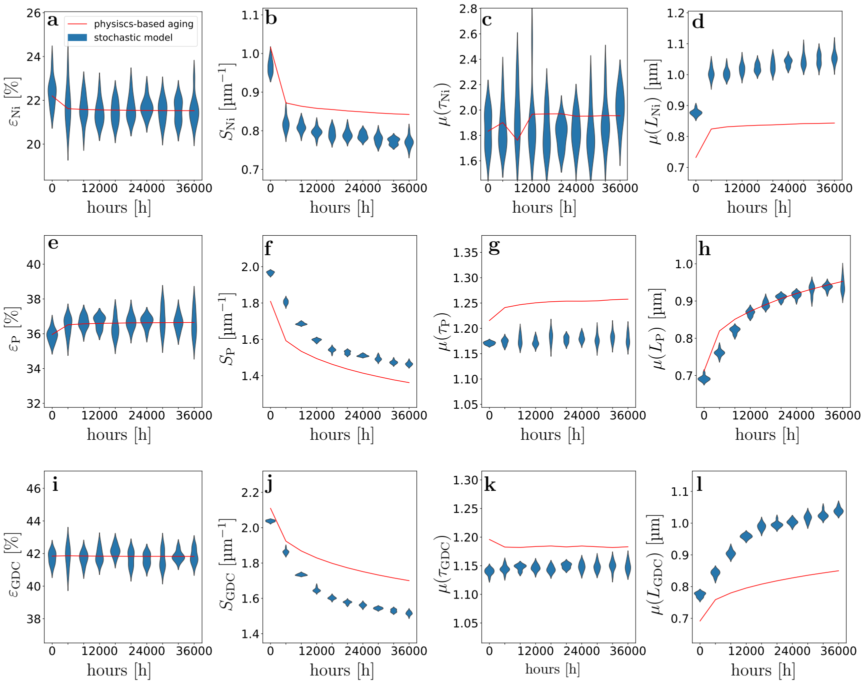

Figure 2: Comparison of volume fraction (first column), specific surface area (second column), mean geodesic tortuosity from TPB (third column), and mean chord length (fourth column) of the three phases, i.e. nickel (top row), pore space (middle row) and GDC (bottom row), computed for the image data obtained by physics-based aging simulations (red), and for 10 realizations drawn from the stochastic 3D model for each duration of aging (blue).

Figure 2 shows the volume fraction, the specific surface area, the mean geodesic tortuosity from TPB, and the mean chord length of the three phases nickel, pores, and GDC after every 4000 hours of aging for 10 realizations of the stochastic 3D model, where the results obtained are displayed as violin plots. These plots allows for intuitive interpretation of data distribution, as the width and shape of the violin directly show where values are clustered or rare. In addition, results are shown that are obtained for these geometrical descriptors by physics-based aging simulations. Note that although also in the latter case the results are computed only at discrete time points, they are represented here as a continuous line for better visualization.

It turns out that for the nickel phase and the pore space, the specific surface areas (SSAs) computed from the stochastic model realizations coincide well with the corresponding results obtained from the physics-based aging simulations, see Figures 2b and 2f, while the SSA of the GDC phase is slightly underestimated by the stochastic 3D model. Similarly, the mean geodesic tortuosity of the pore space and the GDC phase is slightly underestimated but all in all reproduced well with a small MAPE as can be seen in Table 2. Furthermore, as can be seen in Figure 2c, the mean geodesic tortuosity of the nickel phase fluctuates over various aging durations and no particular trend can be seen in physics-based aging either. This is caused by the poor connectivity of the nickel phase. In particular, the average volume fraction of the percolating phase of the 77 physics-based aging simulations has a share of 4.48 %.

In Figure 3 results are visualized that have been obtained for the specific length of the TPB and the SSA of the DPB. As shown in Figure 3a, the stochastic 3D model captures the general decline in the specific length of the TPB, where it tends to slightly underestimate the TPB length, with MAPE of 6.67 % across all aging durations, compared to the results obtained by the physics-based aging simulations. However, the values for the SSA of DPB obtained by the stochastic 3D model coincide quite well with those of the physics-based aging simulations, see Figure 3b, with MAPE of 2.60 % across all aging durations.

All in all, with respect to most geometrical descriptors, the realizations drawn from the stochastic 3D model coincide well with the images obtained by physics-based aging simulations. Larger deviations can only be observed in the mean chord length of the nickel and GDC phases. Given the small number of model parameters and the fact that the same model type is used for all aging durations, the stochastic model achieves satisfactory results based on the remaining geometric descriptors, i.e, the SSA, the mean geodesic tortuosity, the specific length of TPB and the SSA of DPB. Thus, the low-parametric model introduced in Section 3.2 is suitable for fast simulation of 3D morphologies of SOFC anodes for all relevant aging durations.

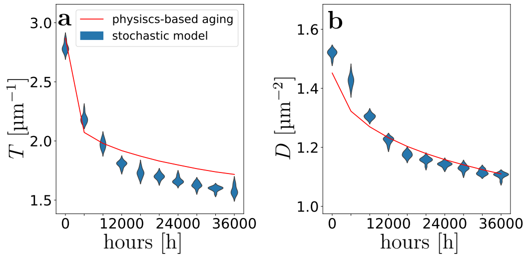

Figure 3: Comparison of the specific length of the TPB (a) and the SSA of the DPB (b) obtained by physics-based aging simulations (red), and for 10 realizations drawn from the stochastic 3D model for each duration of aging (blue).

4.2 Predictive simulation

We now show how the stochastic model introduced in Section 3.2 can be used to generate 3D morphologies of SOFC anodes for aging durations for which no physics-based aging simulations have been performed. This is achieved using the regression functions given in Eq. (8) and solving the optimization problem stated in Eq. (9). To evaluate the robustness of the prediction, the four-dimensional parameter vector $a = (a_1, a_2, a_3, a_4) \in \mathbb{R}^4$ of the regression function f_a is adjusted on the basis of numerical aging simulations for different aging durations. Specifically, we use the (optimized) parameter vector a^* derived from physics-based aging simulations up to 4000 h, 9500 h, 19 000 h, 28 500 h and 38 000 h, respectively, and compare the geometrical descriptors of the 3D images drawn from the correspondingly fitted stochastic models with those obtained by physics-based aging simulations.

To fit the regression function given in Eq. (8), the parameters $\theta_{t,1}, \ldots, \theta_{t,6} \in \mathbb{R}$ for all $t \in \mathcal{T}$ of the stochastic 3D models, which are calibrated by the outputs of each of the 77 physics-based aging simulations, are used as ground truth. Although these parameters are determined only for discrete time points $t \in \mathcal{T}$, they are represented in Figure 4 as continuous (red) lines for better visualization. In particular, as the model parameter $\beta_X (= \theta_{t,5})$ of the covariance function ρ_X introduced in Eq (1), which equals the fifth entry of the six-dimensional parameter vector of the stochastic 3D microstructure model, is almost constant over time (see Figure 4d), we use the mean of the observed values of β_X for all aging durations $t \in \mathcal{T}$. To determine the evolution of the remaining five model parameters in continuous time, the regression function given in Eq. (8) is applied. Thus, the parameter vector a^* derived from physics-based aging simulations up to 4000 h, 9500 h, 19 000 h, 28 500 h, 38 000 h, respectively, is used to construct a time-continuous representation of the evolution of the j-th model parameter via $\theta_{t,j} = f_{a^*}(t)$ for all $t \geq 0$ and $j \in \{1, \ldots, 4\} \cup \{6\}$, see Figure 4. For the threshold $\lambda_Z (= \theta_{t,1})$ and the covariance parameter $\alpha_X (= \theta_{t,3})$ only small differences can be seen for the different aging durations up to 4000 h, 9500 h, 19 000 h, 28 500 h, 38 000 h, respectively. The differences for $\lambda_Y, \alpha_Y, \beta_Y$ are more pronounced, where the results for β_Y are particularly striking, as a different trend appears during the initial hours. However, for physics-based aging simulations up to longer aging durations, the regression function f_{a^*} approximates the ground truth increasingly well.

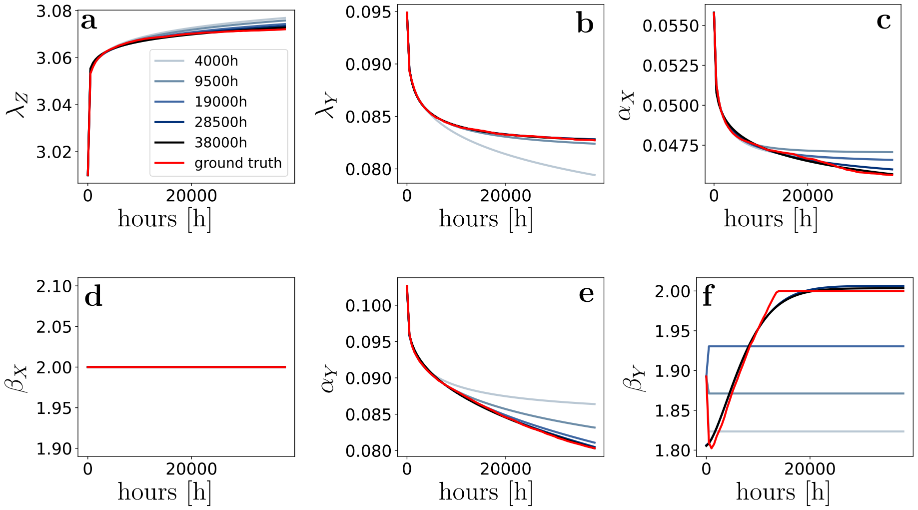

Figure 4: Time-continuous representation of the evolution of model parameters by regression functions fitted to physics-based aging simulations up to 4000 h, 9500 h, 19 000 h, 28 500 h (blue lines, with increasing darkness) and 38 000 h (dark), respectively.

To get a visual impression of the situation for subsequent aging durations, we simulated 3D morphologies of SOFC anodes up to an aging duration of 45 000 h, using stochastic 3D models based on the parameter vector a^* derived from physics-based aging simulations up to different aging durations; see Figure 5. For better visualization, 2D slices of these 3D morphologies are also shown.

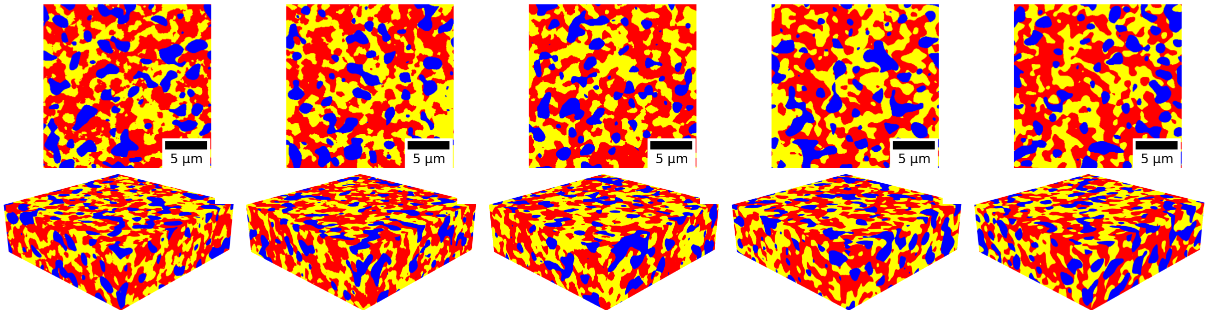

(a) (b) (c) (d) (e)

Figure 5: Predictive simulation of 3D morphology (20 µm × 6.35 µm × 20 µm) and 2D slices (20 µm × 20 µm)after 45 000 h of the stochastic model calibrated to aging durations up to 4000 h (a), 9500 h (b), 19 000 h (c), 28 500 h (d) and 38 000 h (e).

After an initial visual impression, we further investigate the influence of the regression functions shown in Figure 4 on the 3D morphologies of SOFC anodes generated by the correspondingly fitted stochastic 3D models. For this, we compute the geometrical descriptors given in Table 1 every 2000 hours up to 38,000 hours, where the averages of 10 model realizations with a size of 20 µm in each direction are used. In addition, the geometrical descriptors for the physics-based aging simulations are computed (red lines); see Figure 6. Here, the results are shown which have been obtained for the volume fraction, specific surface area, mean geodesic tortuosity from TPB and mean chord length of the three phases nickel, pores, and GDC. Note that in all cases, the geometrical descriptors are computed only for a few discrete time points. However, like in the previous figures, continuous lines are used in Figure 6 for visualization purposes. For most geometrical descriptors, the differences between the stochastic models based on different aging simulations are small. But, as can be seen in Figures 6f and 6h for the specific surface area and mean chord length of the pore space, longer physics-based aging simulations up to 28 500 h lead to better results. After that, no more differences between these geometrical descriptors of the stochastic 3D models can be observed. In contrast, surprisingly enough, it turns out that for the specific surface area and the mean chord length of the GDC phase, shorter aging durations lead to better results; see Figures 6j and 6l. Note that the large deviations for the mean geodesic tortuosity of the nickel phase starting from TPB (see Figure 6c) can again be attributed to the poor connectivity of the nickel phase.

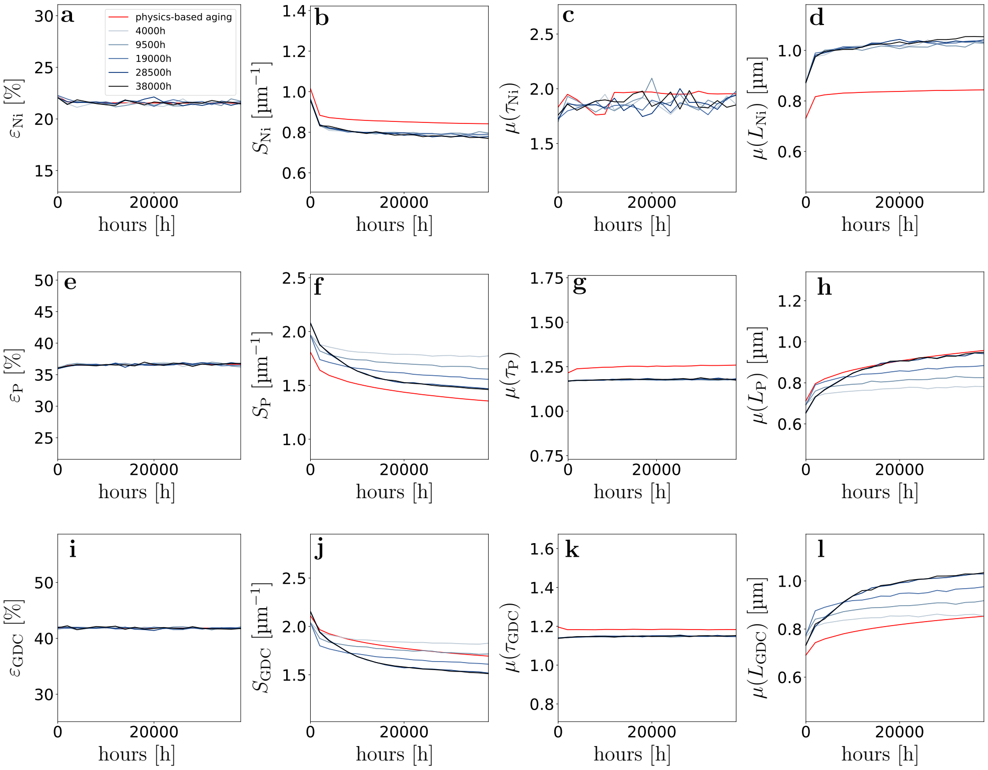

Figure 6: Evaluation of the robustness of predictive simulations of the 3D morphology of SOFC anodes, using regression functions fitted to physics-based aging simulations up to 4000 h, 9500 h, 19 000 h, 28 500 h (blue lines, with increasing darkness) and 38 000 h (dark), respectively, where the geometrical descriptors are computed for nickel (top row), pore space (middle row) and GDC (bottom row). The red lines show the descriptors computed for the physics-based aging simulations.

In Figure 7, the results are visualized that have been obtained for the specific length of the TPB and the specific surface area of DPB of the stochastic 3D models based on the regression parameter vectors a^* derived from physics-based aging simulations up to 4000 h, 9500 h, 19 000 h, 28 500 h and 38 000 h. In both cases, longer physics-based aging simulations tend to lead to better results. However, the stochastic 3D models calibrated for aging durations up to 28 500 h and 38 000 h, respectively, exhibit only negligible differences. Moreover, the model calibrated up to

19 000 h shows only small variations in the geometrical descriptors compared to the models calibrated up to 28 500 h and 38 000 h. This means that the physics-based aging simulation up to an aging duration of 19 000 h is sufficient to accurately predict the microstructure evolution up to 38 000 h. Most model parameter changes take place within the first 19 000 h, allowing for a reliable estimation of the following exponential behavior.

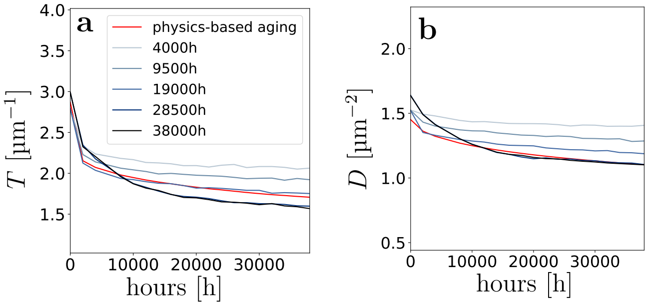

Figure 7: Evaluation of the robustness of predictive simulations of TPB and DPB, using regression functions fitted to physics-based aging simulations up to 4000 h, 9500 h, 19 000 h, 28 500 h (blue lines, with increasing darkness) and 38 000 h (dark), respectively, where the geometrical descriptors are computed for nickel (top row), pore space (middle row) and GDC (bottom row). The red lines show the descriptors computed for the physics-based aging simulations.

4.3 Regression formulas for expressing geometrical descriptors by model parameters

In this section, regression formulas are derived for S_i, $\mu(\tau_i)$, and $\mu(L_i)$, where $i \in \{\text{Ni, P, GDC}\}$, as well as for T and D, based on the parameters of the stochastic 3D model. Therefore, we generate a large set of different virtual microstructures, drawing samples from the given stochastic 3D model and systematically vary the model parameters.

However, note that for the volume fractions ε_{Ni}, ε_{P} and ε_{GDC} we do not derive analytical regression formulas to express these geometrical descriptors by parameters of the stochastic 3D model. For simplicity, we systematically vary the volume fractions ε_{Ni} and ε_P and convert them to the corresponding threshold values using Eqs. (3) and (4), instead of directly varying the threshold parameters λ_Z and λ_Y. More precisely, candidates for the volume fractions of the three phases are drawn from a uniform distribution on the interval $[0.1, 0.8]$ and then normalized by their sum, which ensures that the sum of the volume fractions equals 1. If one of the volume fractions is below 0.1, the simulated values are discarded. Otherwise, the volume fractions are used to determine the thresholds λ_Z and λ_Y via Eqs. (3) and (4). Finally, the model parameters α_X and α_Y are uniformly drawn from $[0.045, 0.15]$, while β_X and β_Y are uniformly drawn from $[1.6, 1.99]$. In this way, we generate 2000 different virtual 3D microstructures with a size of 20 µm in each direction.

To derive the regression formulas mentioned above, we employ symbolic regression [55], which is a machine learning approach that identifies analytical formulas best fitting the data. More precisely, we split the set of simulated microstructures, together with the corresponding geometrical descriptors, into training and test sets containing 1340 and 660 cases, respectively. Then, we use the algorithm given in [55] to fit regression formulas for each geometrical descriptor and each complexity up to 15. Note that a lower complexity leads to simpler regression formulas. However, the algorithm used does not guarantee that the units of geometrical descriptors are correctly maintained by the (preliminary) regression formulas. It should be noted that the model parameters α_X and α_Y have the unit µm^{-1}, while all other model parameters are unitless. That is why we exclude all regression formulas that do not match the correct unit. For the remaining formulas, the Akaike information criterion (AIC) [56] is used on the test set, i.e., for each geometrical descriptor, the regression formula with the smallest AIC value is chosen; see Table 3.

Figure 8 shows how well the regression formulas fit the data for the specific surface area, the mean geodetic tortuosity from TPB, and the mean chord length on the test set. Specifically, the geometrical descriptors $S_i, \mu(\tau_i)$ and $\mu(L_i)$ computed from simulated image data are presented, along with their corresponding estimates $\widehat{S}_i, \mu(\widehat{\tau}_i)$ and $\mu(\widehat{L}_i)$ obtained by the regression formulas given in Table 3, for $i \in \{\text{Ni, P, GDC}\}$. The resulting values of the coefficient of determination (R^2) as well as the MAPE can be also found in Figure 8.

phase	geometrical descriptor	regression formula
Nickel	S_{Ni}	$\alpha_X(\lambda_Z - 6.30 + 70.82/\beta_X)$
	$\mu(\tau_{\mathrm{Ni}})$	$\exp((\lambda_Z + 11.41/\exp(\exp(\lambda_Z - 3.18)\beta_X) - 3.07)^{-1})$
	$\mu(L_{\mathrm{Ni}})$	$(0.90/\lambda_Z + \beta_X - 1.29)/\alpha_X$
Pore	S_{P}	$(\lambda_Y - \beta_Y + 4.17)(5.40 - \lambda_Y^2)(\alpha_X + \alpha_Y)$
	$\mu(\tau_{\mathrm{P}})$	$((\lambda_Z + \beta_Y)(1.68 - (2.42 - \lambda_Y)\lambda_Y))^{-1} + 1.02$
	$\mu(L_{\mathrm{P}})$	$\beta_Y/(\exp(\lambda_Y)\alpha_Y - \alpha_X/(\lambda_Z(\beta_X - 0.29)))$
GDC	S_{GDC}	$(\alpha_Y + \alpha_X)((\exp(\lambda_Y) + 22.55)/\beta_X)$
	$\mu(\tau_{\mathrm{GDC}})$	$\exp(1.11/(6.75\exp(\lambda_Y) + \lambda_Z - 2.69))$
	$\mu(L_{\mathrm{GDC}})$	$\beta_Y/(\alpha_Y/\exp(\lambda_Y) + \alpha_X/(0.52\lambda_Z))$
	D	$\alpha_Y((\lambda_Z + 1.47)/\exp((\lambda_Y^2 - 2.23)/\beta_Y))$
	T	$5627.85((\alpha_X/((\beta_Y + \lambda_Z)/\alpha_Y))/(\beta_X + \lambda_Y^2))$

Table 3: Regression formulas to express geometrical descriptors by the parameters of the stochastic 3D model.

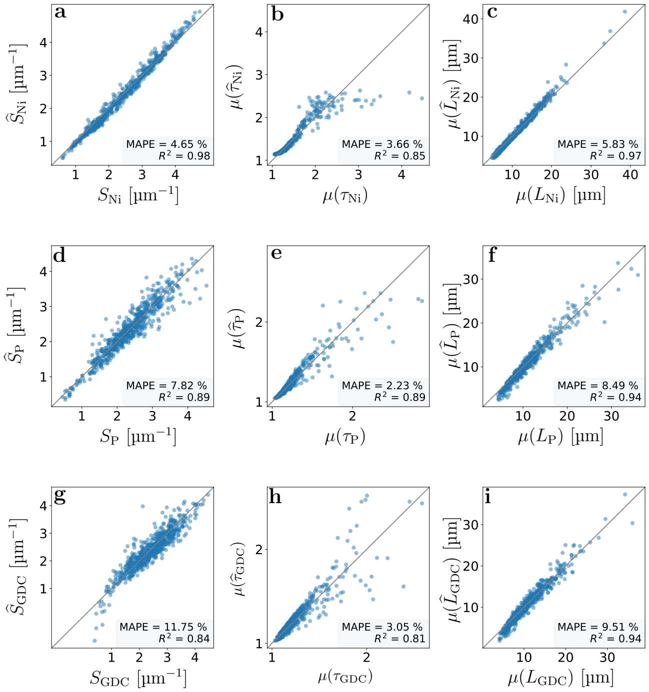

Figure 8: Scatter plots visualizing the values of the geometrical descriptors and their estimates obtained by regression formulas for the nickel phase (top), pore space (middle) and GDC phase (bottom).

As can be seen in Figure 8, the smallest value of R^2 is 0.81 when considering the mean geodesic tortuosity from TPB of the pore space, and the largest value of the MAPE is 11.75 %, which is obtained for the specific surface area of the GDC phase. Thus, all regression formulas given in the upper part of Table 3 capture the relationships between model parameters and geometrical descriptors quite well. Particularly accurate results can be observed for the specific surface area and the mean chord length of the nickel phase. It is also noticeable that the regression formulas for the mean geodesic tortuosity from TPB lead to small MAPE and relatively small R^2 values for all three phases, see Figures 8b, 8e and 8h. This effect is due to the limited variability of the tortuosity values in the test data, which are mostly in a range between 1 and 2. As a result of this low variability, all models with tortuosity values within this interval have good predictive performance. However, larger errors occur when the tortuosity values to be predicted are outside this range.

As the specific length of the TPB and the specific area of the DPB are geometrical descriptors that are crucial for the electrochemical performance of SOFC anodes, it is important to understand the impact the model parameters have on them. According to the formulas given in Table 3, the specific length of the TPB and the specific area of the DPB are influenced by all model parameters. This indicates a rather complex relationship between these two geometrical descriptors and the model parameters. However, as can be seen in Figure 9, the estimates $\widehat{T}$ and $\widehat{D}$ obtained by the regression formulas lead to accurate results for both T and D.

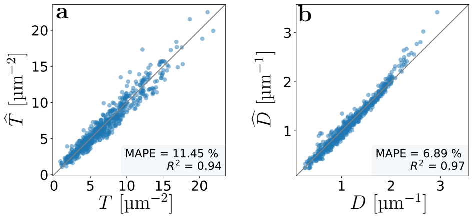

Figure 9: Scatter plots visualizing the specific length T of the TPB and the specific area D of the DPB, together with their estimates $\hat{T}$ and $\hat{D}$ obtained by the regression formulas.

5 Conclusions

In this paper, we combine physics-based aging simulations using a phase-field approach with a stochastic 3D model to generate a wide spectrum of virtual but realistic 3D morphologies of SOFC anodes comprised of nickel, pores, and GDC for different aging durations. The stochastic 3D model is built by excursion sets of two random fields, i.e., a χ^2-field and a Gaussian random field, resulting in six model parameters. For model calibration, formulas are used that express the volume fractions of the three phases and the two-point coverage probabilities by the model parameters. Since the geometrical descriptors appearing in these formulas can be easily computed from image data generated by the physics-based aging simulations, a fast and efficient model calibration is possible. The goodness of the model fit is evaluated by comparing various geometrical descriptors computed from physics-based aging simulations with those obtained for realizations of the stochastic 3D model.

As the model is calibrated for various aging durations, an exponential regression function is used to determine the model parameters in continuous time. This enables us to perform simulations of the 3D morphology of SOFC anodes for unobserved aging durations. To quantify the quality of such predictive simulations, different aging durations are assumed and the 3D morphologies generated by the fitted stochastic 3D models are evaluated through comparison of geometrical descriptors of model realizations and image data obtained by the physic-based aging simulations. The results achieved in this way show that physics-based aging simulations up to 19 000 h are sufficient to reach a sufficiently accurate prediction quality up to 38 000 h. In addition, symbolic regression is used to derive regression formulas that express various geometrical descriptors by the parameters of the underlying stochastic 3D model.

Thus, in the present paper, a comprehensive computational framework of combined physics-based and stochastic modeling is developed to predict the 3D morphology of GDC-based SOFC anodes for various aging durations. In a forthcoming paper, this framework will be used for virtual materials testing, i.e., to quantitatively investigate process-structure-property relationships, which correlate the processing conditions, 3D morphology of SOFC anodes with their effective functional properties.

Data Availability Statement

A selected representative dataset of this work is publicly accessible on ZENODO [57]. The complete datasets are available from the corresponding author on reasonable request.

Acknowledgment

The authors would like to thank the Federal Ministry of Research, Technology and Space (BMFTR) for financial support within the priority program “Mathematics for Innovations” (grant number 05M2022). Contributions to formulate the multiphase-field methodology have been funded by the Helmholtz association, porgramme ”MSE”, no.43.31.01 which is gratefully acknowledged.

References

[1] K. Kendall, M. Kendall, High-Temperature Solid Oxide Fuel Cells for the 21st Century: Fundamentals, Design and Applications, Academic Press, 2015.

[2] N. Brandon, E. Ruiz-Trejo, P. Boldrin, Solid Oxide Fuel Cell Lifetime and Reliability: Critical Challenges in Fuel Cells, Academic Press, 2017.

[3] M. S. Khan, S.-B. Lee, R.-H. Song, J.-W. Lee, T.-H. Lim, S.-J. Park, Fundamental mechanisms involved in the degradation of nickel–yttria stabilized zirconia (Ni–YSZ) anode during solid oxide fuel cells operation: A review, Ceramics International 42 (2016) 35–48.

[4] A. Mai, M. Becker, W. Assenmacher, F. Tietz, D. Hathiramani, E. Ivers-Tiffée, D. Stöver, W. Mader, Time-dependent performance of mixed-conducting SOFC cathodes, Solid State Ionics 177 (2006) 1965–1968.

[5] Y. Liu, M. Juckel, N. H. Menzler, A. Weber, Ni/GDC fuel electrode for low-temperature SOFC and its aging behavior under accelerated stress, Journal of The Electrochemical Society 171 (2024) 054514.

[6] T. Suzuki, Z. Hasan, Y. Funahashi, T. Yamaguchi, Y. Fujishiro, M. Awano, Impact of anode microstructure on solid oxide fuel cells, Science 325 (2009) 852–855.

[7] S. Torquato, Random Heterogeneous Materials: Microstructure and Macroscopic Properties, Springer, 2002.

[8] A. Hauch, S. Ebbesen, S. H. Jensen, M. Mogensen, Solid oxide electrolysis cells: Microstructure and degradation of the Ni/yttria-stabilized zirconia electrode, Journal of the Electrochemical Society 155 (2008) B1184.

[9] F. Tietz, D. Sebold, A. Brisse, J. Schefold, Degradation phenomena in a solid oxide electrolysis cell after 9000 h of operation, Journal of Power Sources 223 (2013) 129–135.

[10] J. Zhang, C. Lenser, N. H. Menzler, O. Guillon, Comparison of solid oxide fuel cell (SOFC) electrolyte materials for operation at 500 °C, Solid State Ionics 344 (2020) 115138.

[11] A. Nenning, C. Bischof, J. Fleig, M. Bram, A. K. Opitz, The relation of microstructure, materials properties and impedance of SOFC electrodes: A case study of Ni/GDC anodes, Energies 13 (2020) 987.

[12] S. Hussain, L. Yangping, Review of solid oxide fuel cell materials: Cathode, anode, and electrolyte, Energy Transitions 4 (2020) 113–126.

[13] Y. Liu, F. Wankmüller, T. P. Lehnert, M. Juckel, N. H. Menzler, A. Weber, Microstructural changes in nickel-ceria fuel electrodes at elevated temperature, Fuel Cells 23 (2023) 430–441.

[14] M. Z. Khan, M. T. Mehran, R.-H. Song, J.-W. Lee, S.-B. Lee, T.-H. Lim, A simplified approach to predict performance degradation of a solid oxide fuel cell anode, Journal of Power Sources 391 (2018) 94–105.

[15] S. Weber, B. Prifling, M. Juckel, Y. Liu, M. Wieler, D. Schneider, B. Nestler, N. H. Menzler, V. Schmidt, Comparing the 3D morphology of solid-oxide fuel cell anodes for different manufacturing processes, operating times, and operating temperatures, Journal of The Electrochemical Society 172 (2025) 044506.

[16] A. Zekri, M. Knipper, J. Parisi, T. Plaggenborg, Microstructure degradation of Ni/CGO anodes for solid oxide fuel cells after long operation time using 3D reconstructions by FIB tomography, Physical Chemistry Chemical Physics 19 (2017) 13767–13777.

[17] A. Sciazko, Y. Komatsu, T. Shimura, N. Shikazono, Multiscale microstructural evolutions of nickel-gadolinium doped ceria in solid oxide fuel cell anode, Journal of Power Sources 478 (2020) 228710.

[18] L. Holzer, B. Münch, B. Iwanschitz, M. Cantoni, T. Hocker, T. Graule, Quantitative relationships between composition, particle size, triple phase boundary length and surface area in nickel-cermet anodes for solid oxide fuel cells, Journal of Power Sources 196 (2011) 7076–7089.

[19] I. Steinbach, F. Pezzolla, A generalized field method for multiphase transformations using interface fields, Physica D: Nonlinear Phenomena 134 (1999) 385–393.

[20] N. Moelans, B. Blanpain, P. Wollants, An introduction to phase-field modeling of microstructure evolution, Calphad - Computer Coupling of Phase Diagrams and Thermochemistry 32 (2008) 268–294.

[21] B. Nestler, A. Choudhury, Phase-field modeling of multi-component systems, Current Opinion in Solid State and Materials Science 15 (2011) 93–105.

[22] A. Prahs, D. Schneider, B. Nestler, A continuum thermodynamic approach to the phase-field method: the order parameter as internal state variable, Continuum Mechanics and Thermodynamics 37 (2025) 55.

[23] L.-Q. Chen, Phase-field models for microstructure evolution, Annual Review of Materials Research 32 (2002) 113–140.

[24] H.-Y. Chen, H.-C. Yu, J. S. Cronin, J. R. Wilson, S. A. Barnett, K. Thornton, Simulation of coarsening in three-phase solid oxide fuel cell anodes, Journal of Power Sources 196 (2011) 1333–1337.

[25] Q. Li, L. Liang, K. Gerdes, L.-Q. Chen, Phase-field modeling of three-phase electrode microstructures in solid oxide fuel cells, Applied Physics Letters 101 (2012) 033909.

[26] Z. Jiao, N. Shikazono, Simulation of the reduction process of solid oxide fuel cell composite anode based on phase field method, Journal of Power Sources 305 (2016) 10–16.

[27] Y. Lei, T.-L. Cheng, H. Abernathy, W. Epting, T. Kalapos, G. Hackett, Y. Wen, Phase field simulation of anode microstructure evolution of solid oxide fuel cell through $Ni(OH)_2$ diffusion, Journal of Power Sources 482 (2021) 228971.

[28] S. Yang, J. Gao, M. Trini, S. De Angelis, P. S. Jørgensen, J. R. Bowen, L. Zhang, M. Chen, Ni coarsening in Ni-yttria stabilized zirconia electrodes: Three-dimensional quantitative phase-field simulations supported by ex-situ ptychographic nano-tomography, Acta Materialia 246 (2023) 118708.

[29] Y. Lei, Y. A. Mantz, W. A. Saidi, H. W. Abernathy, Y. Wen, Ni coarsening under humid atmosphere in the electrode of solid oxide cells: A combined study of density-functional theory and phase-field modeling, Journal of Power Sources 613 (2024) 234778.

[30] A. Choudhury, B. Nestler, Grand-potential formulation for multicomponent phase transformations combined with thin-interface asymptotics of the double-obstacle potential, Physical Review E 85 (2012) 021602.

[31] P. W. Hoffrogge, A. Mukherjee, E. Nani, P. K. Amos, F. Wang, D. Schneider, B. Nestler, Multiphase-field model for surface diffusion and attachment kinetics in the grand-potential framework, Physical Review E 103 (2021) 033307.

[32] P. W. Hoffrogge, D. Schneider, F. Wankmüller, M. Meffert, D. Gerthsen, A. Weber, B. Nestler, M. Wieler, Performance estimation by multiphase-field simulations and transmission-line modeling of nickel coarsening in FIB-SEM reconstructed Ni-YSZ SOFC anodes I: Influence of wetting angle, Journal of Power Sources 570 (2023) 233031.

[33] M. Sun, A. Li, X. Zhang, Y. Fei, L. Zhu, Z. Huang, Microstructure evolution and performance evaluation of nickel/gadolinium-doped ceria fuel electrode for solid oxide fuel cell investigated by integrated meso-scale modeling, Preprint at SSRN (2024). `doi:http://dx.doi.org/10.2139/ssrn.5037533`.

[34] R. K. Jeela, M. Ahmad, M. Wieler, Y. Liu, M. Juckel, D. Schneider, A. Weber, N. H. Menzler, B. Nestler, Multiphase-field simulation studies of coarsening in Ni-GDC SOFC anode microstructures and the effect of interfacial energies, ACS Applied Energy Materials (2025) in print.

[35] R. K. Jeela, G. Tosato, M. Ahmad, M. Wieler, A. Koeppe, B. Nestler, D. Schneider, Enhancing solid oxide fuel cells development through Bayesian active learning, Advanced Energy Materials 15 (2025) 2501216.

[36] M. Neumann, M. Osenberg, A. Hilger, D. Franzen, T. Turek, I. Manke, V. Schmidt, On a pluri-Gaussian model for three-phase microstructures, with applications to 3D image data of gas-diffusion electrodes, Computational Materials Science 156 (2019) 325–331.

[37] P. Marmet, L. Holzer, T. Hocker, V. Muser, G. K. Boiger, M. Fingerle, S. Reeb, D. Michel, J. M. Brader, Stochastic microstructure modeling of SOC electrodes based on a pluri-Gaussian method, Energy Advances 2 (2023) 1942–1967.

[38] M. Neumann, B. Abdallah, L. Holzer, F. Willot, V. Schmidt, Stochastic 3D modeling of three-phase microstructures for predicting transport properties: A case study, Transport in Porous Media 128 (2019) 179–200.

[39] H. Moussaoui, J. Laurencin, Y. Gavet, G. Delette, M. Hubert, P. Cloetens, T. Le Bihan, J. Debayle, Stochastic geometrical modeling of solid oxide cells electrodes validated on 3D reconstructions, Computational Materials Science 143 (2018) 262–276.

[40] M. Neumann, S. E. Wetterauer, M. Osenberg, A. Hilger, P. Gräfensteiner, A. Wagner, N. Bohn, J. R. Binder, I. Manke, T. Carraro, V. Schmidt, A data-driven modeling approach to quantify morphology effects on transport properties in nanostructured nmc particles, International Journal of Solids and Structures 280 (2023) 112394.

[41] B. Prifling, M. Ademmer, F. Single, O. Benevolenski, A. Hilger, M. Osenberg, I. Manke, V. Schmidt, Stochastic 3D microstructure modeling of anodes in lithium-ion batteries with a particular focus on local heterogeneity, Computational Materials Science 192 (2021) 110354.

[42] J. Feinauer, T. Brereton, A. Spettl, M. Weber, I. Manke, V. Schmidt, Stochastic 3D modeling of the microstructure of lithium-ion battery anodes via Gaussian random fields on the sphere, Computational Materials Science 109 (2015) 137–146.

[43] O. Stenzel, O. Pecho, L. Holzer, M. Neumann, V. Schmidt, Big data for microstructure-property relationships: A case study of predicting effective conductivities, AIChE Journal 63 (2017) 4224–4232.

[44] M. Neumann, O. Stenzel, F. Willot, L. Holzer, V. Schmidt, Quantifying the influence of microstructure on effective conductivity and permeability: Virtual materials testing, International Journal of Solids and Structures 184 (2020) 211–220.

[45] A. Elmoghazy, S. Weber, R. Jeela, A. Prahs, B. Prifling, D. Schneider, V. Schmidt, B. Nestler, Investigations on the microstructural degradation and mechanical response of Ni–CGO anodes using the phase-field method and stochastic models.Working paper (under preparation) (2025).

[46] Pace3D (Parallel Algorithms for Crystal Evolution in 3D), https://www.h-ka.de/idm/profil/pace3d-software#c17811, Accessed: 13.11.2025.

[47] M. Seiz, P. Hoffrogge, H. Hierl, A. Reiter, D. Schneider, B. Nestler, Phase-field simulations with the grand potential approach, in: High Performance Computing in Science and Engineering'20: Transactions of the High Performance Computing Center, Stuttgart (HLRS) 2020, Springer, 2021, pp. 561–577.

[48] S. N. Chiu, D. Stoyan, W. S. Kendall, J. Mecke, Stochastic Geometry and Its Applications, 3rd Edition, J. Wiley & Sons, 2013.

[49] R. J. Adler, The Geometry of Random Fields, J. Wiley & Sons, 1981.

[50] C. Lantuéjoul, Geostatistical Simulation: Models and Algorithms, Springer, 2013.

[51] I. Molchanov, Theory of Random Sets, Springer, 2005.

[52] J. Ohser, K. Schladitz, 3D Images of Materials Structures: Processing and Analysis, J. Wiley & Sons, 2009.

[53] A. Quarteroni, R. Sacco, F. Saleri, Numerical Mathematics, Springer, 2007.

[54] M. A. Branch, T. F. Coleman, Y. Li, A subspace, interior, and conjugate gradient method for large-scale bound-constrained minimization problems, SIAM Journal on Scientific Computing 21 (1999) 1–23.

[55] M. Cranmer, Interpretable machine learning for science with PySR and SymbolicRegression.jl, arXiv preprint 2305.01582 (2023).

[56] K. P. Burnham, D. R. Anderson, Model Selection and Multimodel Inference – A Practical Information-Theoretic Approach, Springer, 2002.

[57] S. Weber, B. Prifling, R. K. Jeela, A. Prahs, D. Schneider, B. Nestler, V. Schmidt, A time-continuous approach to analyzing anode aging in solid-oxide fuel cells via stochastic 3d microstructure modeling and physics-based simulations [data set]. `doi:https://doi.org/10.5281/zenodo.17748893`.